



# Effects of aspect ratio and orientation on the wake characteristics of low Reynolds number flow over a triangular prism



S. Ganga Prasath<sup>a</sup>, M. Sudharsan<sup>a</sup>, V. Vinodh Kumar<sup>b</sup>,  
S.V. Diwakar<sup>b</sup>, T. Sundararajan<sup>b</sup>, Shaligram Tiwari<sup>b,\*</sup>

<sup>a</sup> Indian Institute of Information Technology, Design & Manufacturing, IIT Madras Campus, Chennai 600036, India

<sup>b</sup> Department of Mechanical Engineering, IIT Madras, Chennai 600036, India

## ARTICLE INFO

### Article history:

Received 18 July 2012

Accepted 29 December 2013

Available online 2 February 2014

### Keywords:

Triangular prism

Aspect ratio

Critical Reynolds number

Fixed-grid simulation

Wake characteristics

Hydrodynamic forces

## ABSTRACT

The wake characteristics of unconfined flows over triangular prisms of different aspect ratios have been numerically analysed in the present work. For this purpose, a fixed Cartesian-grid based numerical technique that involves the porous medium approach to mimic the effect of solid blockage has been utilised. Correspondingly, laminar flow simulations ranging from the sub-critical regime (before the onset of vortex shedding) to the super-critical regime have been considered here within the limits of two-dimensionality. In the sub-critical regime, correlations relating the wake bubble length with Reynolds number ( $Re$ ) have been proposed for various aspect ratios. Also, the effects of aspect ratio and Reynolds Number on the drag force coefficient ( $C_D$ ) have been characterised for two different geometrical orientations of the prism (base or apex facing the flow). Subsequently, the critical Reynolds number at the onset of vortex shedding has been predicted for each of the aspect ratio considered, by an extrapolation procedure. The unsteady flow characteristics of the super-critical regime are finally highlighted for different aspect ratios and triangular orientations considered in the study.

© 2014 Elsevier Ltd. All rights reserved.

## 1. Introduction

In the event of flow around bluff bodies, the persistent non-linear fluid structure interactions result in the manifestation of diverse flow behaviour occurring at different ranges of parameters and structural configurations. Generally, these flows are characterised by the presence of a low-pressure wake region (pocket of recirculating low momentum fluid behind the bluff body) that determines the overall flow dynamics. At lower values of Reynolds number ( $Re$ ), this wake region is stably enclosed between the separated streamlines of the free stream. However, with the increase in  $Re$ , the wake bubble undergoes a stream-wise elongation due to viscous stresses and becomes vulnerable to the shear layer instabilities acting on its interface with the free stream. Finally at a critical value of  $Re$ , the wake breaks up and starts to shed eddies that form the von Karman vortex street. As a consequence of these events, the bluff body is subjected to fluctuating drag and lift forces and a corresponding momentum defect is introduced into the fluid stream. This initial transition has further supplements at higher  $Re$  where the route to turbulence is attained via various modes of shear layer and boundary layer modifications.

Various classical reviews have well elucidated the critical features exhibited by the wake of circular cylinders (Zdravkovich, 1990, 1997; Williamson, 1989, 1996; Thompson et al., 2001; Sumner, 2010). These features include the

\* Corresponding author.

E-mail addresses: [shaligt@iitm.ac.in](mailto:shaligt@iitm.ac.in), [shalig.physics@gmail.com](mailto:shalig.physics@gmail.com) (S. Tiwari).

Nomenclature		$\zeta$	grid density
		$\lambda$	porosity
AR	aspect ratio	$\mu$	dynamic viscosity
C	computational constant	$\rho$	fluid density
$C_D$	drag coefficient	$\sigma$	stress
$C_L$	lift coefficient	$\Omega$	computational domain
D	base of triangular prism		
F	volume fraction; hydrodynamic force	Subscripts	
h	height of triangle	bp	base pressure
H	height of the computational domain	cr	critical
k	ratio of dimensionless wake bubble length to Re	D	drag
L	length	f	fluid
n	normal	L	lift
p'	pressure correction	max	maximum
q	computational constant	r	recirculation
Re	Reynolds number ( $\rho u_\infty D / \mu$ )	rms	root mean square
$\bar{S}$	momentum sink	s	solid
t*	non-dimensional time ( $tU/D$ )	$\infty$	free-stream
u	horizontal velocity component		
v	vertical velocity component	Superscripts	
x	horizontal coordinate	ij	cell index
y	vertical coordinate	n	present time step
Greek			
$\Gamma$	control volume		

diverse modes of vortex shedding, laminar to turbulent transition, presence of intermittent oblique eddies and their resultant effects on the base pressure coefficient ( $C_{bp}$ ), etc. Although some of the above effects are also observed for bodies of other cross-sections, each of them is abundant with its own unique flow characteristics. In many cases, the flow separation points in the rear region of the bluff body act as sources of disparities in the downstream flow behaviour. Specifically, for circular cylinders, the points of flow separation strongly depend on the value of Re. On the other hand, for square cylinders, the flow separation normally takes place at its corners. Despite this, a strong relationship between the force coefficients and Re is observed for these cases, more specifically for bluff rectangular cylinders (Davis and Moore, 1982). Similar interesting but distinct features are also exhibited in the case of triangular cylinders. Here, at higher Re and increased bluntness, the fluctuating force coefficients are mainly dominated by the form drag over the skin friction drag. This happens even though the flow separation points are always located at the corners of the base (for both the cases of base and apex facing the approach flow). Additional distinctions are also evident from the fact that critical Re is lower for triangular cylinders (De and Dalal, 2006; Zielinska and Wesfreid, 1995) as compared to that of an equivalent square cylinder (Kelkar and Patankar, 1992).

Even though the existing research publications rigorously bring out various distinctions of flow over circular and square cylinders, the scenario with respect to triangular cylinders (Zeitoun et al., 2011; Srikanth et al., 2010; De and Dalal, 2006, 2007) seems to be less explored. Precisely for the latter systems, the analysis of flow behaviour has often been restricted to equilateral triangles where linear relationship persists (De and Dalal, 2006) between the dimensionless wake bubble length ( $L_w$ ) and Re in the sub-critical regime (before the onset of vortex shedding). Akin to the case of square cylinders, no secondary bifurcations have been observed within the range of Re between 80 and 200. Also, the global modes in the wake region are characterised by the occurrence of a definite maximum in the amplitude at a particular wake location (Zielinska and Wesfreid, 1995). This maximum amplitude is a function of Re near the critical range and has been suitably exploited by Zielinska and Wesfreid (1995) for the accurate evaluation of critical Re.

Although, many of the above features of triangular cylinder are also observed for other cross-sections like circle and square, its actual uniqueness is revealed when there is a change in its aspect ratio or orientation. For instance, Bao et al. (2010) have observed that for an inclination of  $0^\circ$  (where base of the triangle faces the approach flow), the shed vortices combine to form a bigger eddy whose characteristics are different from those behind an equivalent circular cylinder. At other inclinations, the asymmetry of the cylinder with respect to the approaching flow has its notable influence on the mean forces (Lungu and Buresti, 2009). Particularly at  $90^\circ$  inclination angle (where the base of the triangle is parallel to the approaching flow), the system depicts a flat plate behaviour on one side and a sharp edge behaviour on the other (Srigrarom and Koh, 2008). The implications of aspect ratio effects on the triangular systems are evident from the work of Abbassi et al. (2001) where

improvement of heat transfer characteristics was specifically observed for the case of isosceles triangular prism. Thus, a proper characterisation of the geometric influence is warranted both for the sake of its rich physics and also for its potential applications. Since, there is a definite dearth of literature that deals with a variety in geometric configurations (i.e. different orientations and aspect ratios) of triangular prisms, the current analysis aims to address some of their features numerically.

Correspondingly, the present study focuses on the effects of aspect ratio and orientation on dynamic wake characteristics and non-linear hydrodynamic force coefficients, at low Reynolds numbers. In particular, the whole flow behaviour is investigated for aspect ratios varying between 0.5 and 5, and for two different orientations where the apex or the base faces the approaching flow. The numerical methodology used here involves fixed Cartesian grids and a porous medium approach to implicitly emulate the effect of solid structures in the flow field. The resultant hydrodynamic forces acting on the triangular cylinders are evaluated through a generalised approach involving the integration of Navier–Stokes equations over an ‘enclosing control volume’. In addition, the critical Re values for different aspect ratios and configurations are obtained by using the extrapolation technique of Zielinska and Wesfreid (1995).

## 2. Computational model

### 2.1. Fixed grid modelling

The conventional approaches involved in the simulation of bluff body aerodynamics generally utilise a structured or an unstructured mesh that conforms to the shape of the object under investigation (i.e., the bluff body’s surface forms a part of the computational domain boundary). Correspondingly, any movement of the solid object is incorporated here through the use of moving grid methods that suitably realign the body-fitted mesh in tune with the dynamics of the solid structure. The actual flow field is then computed by mapping the changing physical domain onto a fixed computational domain using a time-dependent coordinate transformation (Shanks and Thompson, 1977). Understandably, the limitations associated with the moving grid methods include the computational effort required for coordinate transformation during each time step and the errors that generally accrue due to the field interpolation process. Major challenges are also encountered in the representation of complex solid shapes as well as their subsequent transformations. However, these shortcomings can at times be overcome by the use of fixed grid methods which involve special schemes on a non-deformable grid. Notable of them includes the immersed boundary (IB) method of Peskin (1972) which uses a Cartesian grid that spans over the entire domain (including both the solid and fluid regions of interest) and explicitly represents the solid structure by Lagrangian marker points. The effect of singular force acting on the markers is spread to the surrounding grid points by using discrete Dirac delta functions. Although the IB method was originally developed to simulate flows with immersed elastic boundaries, subsequent modifications have enabled it to handle the scenarios of rigid boundaries like the flow over stationary circular cylinders (Lai and Peskin, 2000). However, as shown by Goldstein et al. (1993), issues in these methods primarily arise due to the imposition of forcing terms on selected boundary points that gives rise to spurious flow fields within the confines of the solid boundary (Su et al., 2007). One of the possible ways of remedying this issue involves the fictitious domain approach (Angot et al., 1999; Khadra et al., 2000) where the total flow domain is considered as Navier–Stokes/Brinkman governed porous media (Brinkman, 1949). The effects of the solid structures are emulated here through a porous body resistance term, with permeability approaching infinity for the fluid phase and zero for the fully solid region.

In the current work, the main objective of simulating flow over triangular prisms is achieved by extending the fictitious domain model of Sinha et al. (1992) and Voller and Prakash (1987) where the volumetric forcing term is related to the local solid fraction via the Carman–Koseny equation (Carman, 1937). Here, a known configuration of solid bodies is first converted into an equivalent discrete form of local solid fractions  $F_s$  ( $F_s = 1 - \lambda$ , where  $\lambda$  is the porosity) by geometrically estimating the truncated solid area in each computational cell. Based on this solid fraction, a momentum source ( $\vec{S}$ ) is obtained for each computational cell through the Carman–Koseny expression, which is given as

$$\vec{S} = C \frac{F_s^2 \vec{U}}{(1 - F_s)^3 + q}, \quad (1)$$

where  $q$  is a computational constant ( $=0.001$ ) introduced to prevent division by zero in the solid region and the value of  $C$  is chosen as  $1.6 \times 10^6$ . The forcing term  $\vec{S}$  acts as a momentum sink and facilitates the conversion of constituent laws in the individual media into a unified conservation equation for the domain  $\Omega$  as given below:

$$\rho \left( \frac{\partial \vec{U}}{\partial t} + \vec{U} \cdot \nabla \vec{U} \right) = -\nabla p + \vec{\nabla} \cdot \left[ \mu \left( \vec{\nabla} \vec{U} + \nabla \vec{U}^T \right) \right] - \vec{S} \quad \text{in } \Omega. \quad (2)$$

In the above equation,  $p$  represents the gauge pressure and  $\rho$  and  $\mu$  denote the fluid density and the dynamic viscosity, respectively. The primary objective of the porous medium approach adopted here is to provide a smooth transition region of about one cell thickness over which the flow resistance due to blockage varies from zero (in the fluid region) to infinity (in the solid region). Representing the blockage effect in terms of the percentage blockage ( $F_s$ ) instead of the actual geometry of the blockage gives a simple and convenient way to handle flow over any arbitrary shaped solid structure using a Cartesian grid. Since  $S$  is zero in the fluid region, the governing equations are simplified here to the classical Navier–Stokes equations. In the region near the interface, where  $0 < F_s < 1$ , the source terms begin to dominate and the momentum equations approach

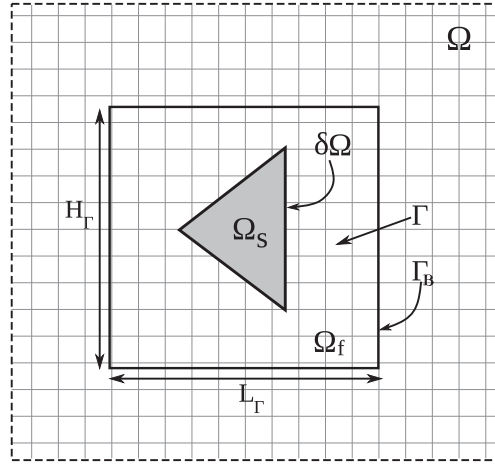


**Fig. 1.** Schematic of flow domain in the proximity of immersed triangular cylinder ( $\Omega_s$  – solid;  $\Omega_f$  – fluid;  $\delta\Omega$  – solid–fluid interface;  $\Gamma$  – enclosing control volume used to evaluate drag and lift forces,  $\Gamma_B$  – boundary of the enclosing control volume,  $\Gamma$ ).

the Darcy law form. When the local solid fraction becomes one, the porous body resistance term dominates over all the other terms in the momentum equations and forces the velocity in the solid region to approach zero value. Even though in principle, the current methodology follows the same approach of IB method by utilising forcing terms for the governing momentum equations, it opts for a volumetric representation unlike the IB method where the forcing on the solid body is at discrete points. Hence, it is possible here to eliminate the occurrence of spurious currents within the solid object. Also, the discrete jump in the characteristics between the solid and fluid regions is confined here within the interfacial cells through the local consideration of Darcy porous media and the Carman–Koseny equation. By the virtue of the latter equation, it may appear that the suitability of the current approach is restricted only for the laminar regime. But in reality, extension of the current model to the turbulent regime is easily achievable through suitable mesh-refinement so that the Darcy porous media of one cell thickness is well encompassed within the laminar sub-layer of the turbulent boundary layer. Besides this, the current approach can also be easily extended to three dimensions since it utilises simple volumetric source terms.

It may be noted that the solid boundary is not identified precisely in the present method and hence, the estimation of drag and lift forces acting on the solid body is achieved here by an alternative means. Correspondingly, the hydrodynamic forces are estimated by integrating the Navier–Stokes equations over the volume  $\Gamma$  which encloses the immersed solid body  $\Omega_s$  as shown in Fig. 1:

$$\vec{F} = - \left[ \iint_{\Gamma} \rho(1-F_s) \frac{\partial \vec{U}}{\partial t} d\Omega + \oint_{\Gamma_B} \rho \vec{U} (\vec{U} \cdot \vec{n}) dl - \oint_{\Gamma_B} \vec{\sigma} \cdot \vec{n} dl \right]. \quad (3)$$

None of the terms in the above equation depends on the geometry of the immersed solid. Therefore, this method of evaluating hydrodynamic forces is applicable, irrespective of the shape or the location of the solid body inside the enclosing control volume,  $\Gamma$ . This approach can also be extended to simulate flows over vibrating solid structures (Shyamprasad et al., 2011).

## 2.2. Numerical scheme

In the current work, a finite volume method based flow solver has been developed wherein the flux form of governing equations (given below) is marched implicitly in time to compute the evolution of the flow variables.

Continuity equation:

$$\oint \rho (\vec{U} \cdot \vec{n}) dl = 0. \quad (4)$$

Momentum equations:

$$\iint \rho \frac{\partial \vec{U}}{\partial t} d\Omega + \oint \rho \vec{U} (\vec{U} \cdot \vec{n}) dl = \oint (\vec{\sigma} \cdot \vec{n}) dl - \iint \vec{S} d\Omega. \quad (5)$$

In order to obtain proper coupling between the pressure and the velocity field, a semi-staggered arrangement of cells has been used as shown in Fig. 2. Here, the velocity nodes (where the ‘ $u$ ’ and ‘ $v$ ’ velocity components are stored) are located at the cell vertices and the pressure nodes are located at the cell centroids. Such staggering of mesh points results in two varieties of cells, namely, the continuity cells (CELC) and the momentum cells (CELM), whose vertices are the velocity nodes and the pressure nodes respectively. The momentum equation (Eq. (2)) is solved over each momentum cell which has a velocity node at the centre and pressure nodes at the vertices. The discrete volume fraction ( $F_s$ ) used to model the effect

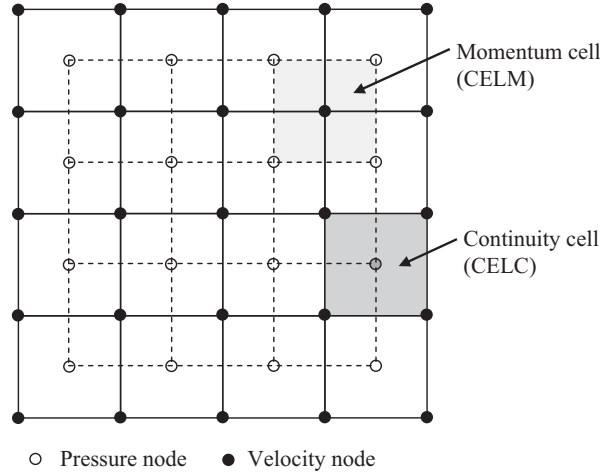


Fig. 2. Schematic of semi-staggered grid arrangement.

of solid blockage (defined below) is geometrically evaluated at the momentum cells and is further substituted in the Carman–Koseny equation to estimate the source terms  $\vec{S}$ :

$$\begin{aligned} F_s &= 1 \quad \forall \text{ cell} \in \Omega_s \\ 0 \leq F_s &\leq 1 \quad \forall \text{ interfacial cells (depending on the fraction of solid within the cell)} \\ F_s &= 0 \quad \forall \text{ cell} \in \Omega_f \end{aligned} \quad (6)$$

Subsequently, the implicitly discretised form of the momentum equation is given as

$$\iint \rho \frac{\vec{U}^{n+1} - \vec{U}^n}{\Delta t} d\Omega + \oint \rho \vec{U}^{n+1} (\vec{U} \cdot \vec{n})^{n+1} dl = \oint (\vec{\sigma} \cdot \vec{n})^{n+1} dl - \iint \vec{S}^{n+1} d\Omega. \quad (7)$$

Here, the nonlinear convective term  $\vec{U}(\vec{U} \cdot \vec{n})$  is linearised using the Picard linearisation procedure and the convective flux is evaluated with an upwind bias, using the QUICK (Quadratic Upstream Interpolation for Convective Kinetics) scheme of Leonard (1979). Since the above equation is solved by considering a guessed pressure field, the resultant velocity  $\vec{U}$  does not satisfy the mass balance. So, Eq. (7) is solved here iteratively in conjunction with the pressure Poisson equation for the continuity cells, which is expressed as

$$\oint \left( \frac{\partial p'}{\partial n} \right) dl = \frac{\rho}{\Delta t} \oint (\vec{U} \cdot \vec{n}) dl. \quad (8)$$

The pressure correction values ( $p'$ ) obtained from Eq. (8) are used to evaluate the correct pressure field and the mass conserving velocity field ( $\vec{U}$ ) in the domain as

$$\vec{U} = \vec{U} - \frac{\Delta t}{\rho} (\nabla p'). \quad (9)$$

In the present work, Incomplete Lower Upper (ILU) pre-conditioned Bi-Conjugate Gradient Stabilised (BiCGStab) linear solver of Van der Vorst (1992) has been used to solve both the pressure correction and the implicitly discretised momentum equations. The iterative procedure is repeated within each time step until the convergence criterion of  $\nabla \cdot \vec{U} \leq 10^{-4}$  is satisfied in every cell of the computational domain. Note that the momentum source term in Eq. (7) is discretised implicitly and so, it favours quicker convergence of the flow field during computations.

### 2.3. Computational domain and boundary conditions

The computational domain used for all the computations in the current work involves a rectangular box of length  $25D$  ( $x = x_{\text{exit}}$ ) and width  $20D$  ( $y = H$ ). The spatial non-dimensionalisation has been achieved by using the base ( $D$ ) of the triangle as the characteristic length. Here, a small rectangular zone enclosing the triangular prism is formed with fine grid spacing. From the boundaries of this bounding box, the grid is stretched (stretching rate = 1.05) gradually to fill up the entire domain, as shown in Fig. 3(b). The boundary conditions employed in the present computations (Fig. 3(a)) are given below:

- Inlet:  $u = u_\infty$  at  $x = 0$ .
- Outlet:  $\partial^2 u / \partial x^2 = 0, \partial^2 v / \partial x^2 = 0$  at  $x = x_{\text{exit}}$ .
- Lateral boundaries:  $\partial u / \partial y = 0, v = 0$  at  $y = 0, H$  (free slip boundaries).

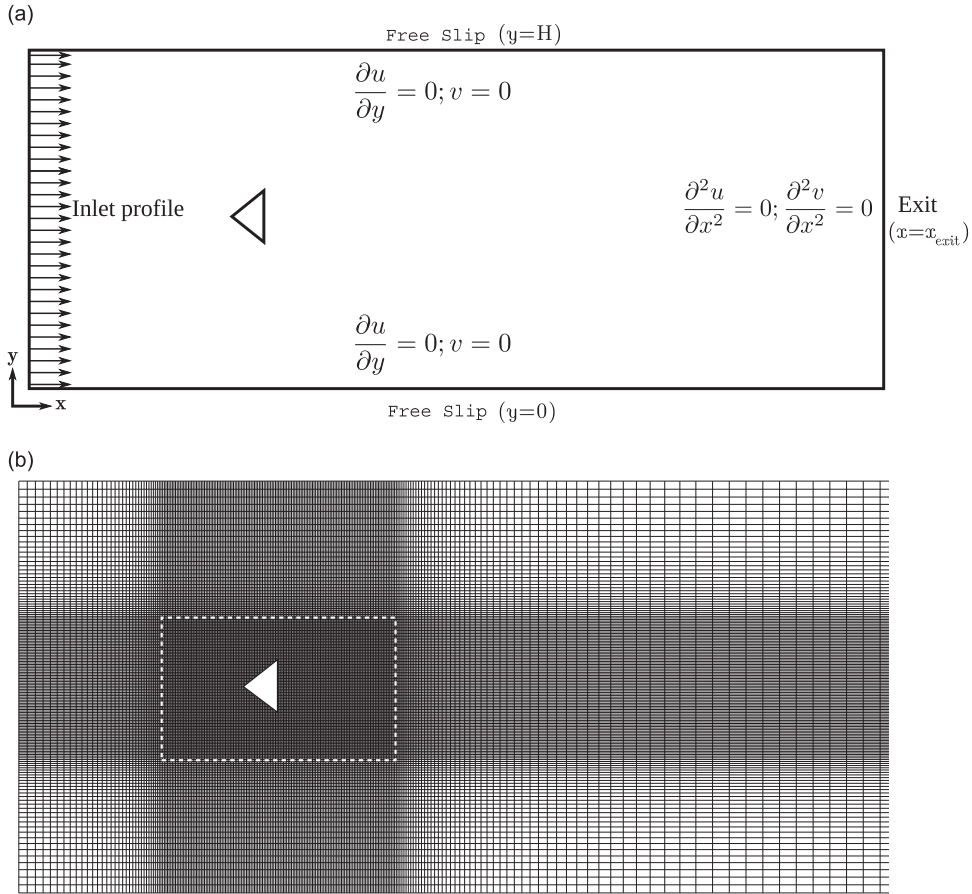


**Fig. 3.** (a) Schematic of the flow domain with the boundary conditions used in the present study. (b) Typical grid used in the simulations (the bounding box is represented by the dashed rectangle).

The triangular prism that is placed inside the rectangular bounding box possesses different aspect ratios (ratio of height ( $h$ ) to the base ( $D$ ) of the triangle) ranging from 0.5 to 5 (0.5, 0.866, 1, 2, 3, 4, 5). As explained earlier, the use of implicit source term ( $\vec{S}$ ) obviates the need for explicit enforcement of boundary condition at the surface of this solid object.

### 3. Validation

In order to assess the capability of the current code, the well established vortex shedding behaviour of stationary circular cylinders has been first studied. The  $C_D$  and  $C_{L,max}$  values obtained from these simulations have been compared with those available in the published literature and are shown in Table 1. The variation of Strouhal number with  $Re$  has been compared with the results of Roshko (1954) and Fey et al. (1998) in Table 2. The closeness of the parameters presented in the tables with those of published literature clearly demonstrates the suitability of the current code in capturing complex flow behaviour arising out of fluid structure interactions. It is to be noted here that the present simulations slightly overpredict, as compared to the data available in the published literature. This is mainly due to the effect of  $\Gamma$  encompassing some extra cells from the fluid region. Correspondingly, any prediction of hydrodynamic forces on  $\Gamma$  includes the effects of viscosity in these cells which make them slightly different from the actual values on  $\Omega_s$ . Hence in order to obtain accurate results,  $\Gamma$  should envelope the immersed solid body as closely as possible. Keeping this in mind, the results in the present work have been obtained by using the smallest possible rectangle around the triangular cylinders.

With regard to the computational time, it is worthy to note that the additional source terms of the unified governing equations are implicitly discretised in the current approach. Hence, the resultant matrix obtained for the evaluation of velocities now possesses better diagonal dominance since the source terms have larger value in the solid region. This eventually enables faster convergence of the BiCGStab algorithm when the velocity matrices are solved. In order to verify this, the Poiseuille flow problem (Fig. 4) similar to the one considered by Silva et al. (2003) has been currently utilised. Here, the no-slip walls for the plane Poiseuille flow have been emulated by considering a thin solid region at the top and the bottom of the domain. For the same mesh size, the present approach yielded an accurate solution (error in peak exit velocity as compared to the exact solution was less than 0.08%) at a CPU time 24% lesser than the usual approach involving just the



**Table 1**

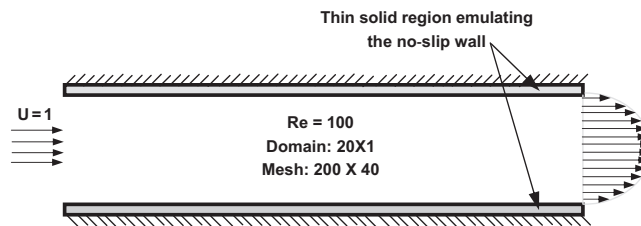
Comparison of mean drag coefficient ( $C_D$ ) and maximum lift coefficient ( $C_{L, \max}$ ) at  $Re=100$  and  $Re=200$  with other numerical results, for flow over a circular cylinder.

Authors	Re = 100		Re = 200	
	$C_D$	$C_{L, \max}$	$C_D$	$C_{L, \max}$
Braza et al. (1986)	1.36	0.25	1.4	0.75
Calhoun (2002)	1.33	0.298	1.17	0.67
Silva et al. (2003)	1.37	–	–	–
Lai and Peskin (2000)	1.44	0.33	–	–
Le et al. (2008)	1.39	0.346	1.38	0.676
Xu and Wang (2006)	1.423	0.34	1.42	0.66
Present	1.44	0.33	1.43	0.68

**Table 2**

Comparison of Strouhal number  $St$  at various  $Re$  with other experimental results.

Re	Roshko (1954)	Fey et al. (1998)	Present
50	0.122	0.122	0.127
80	0.156	0.152	0.158
100	0.167	0.165	0.170
150	0.182	0.184	0.189
200	0.189	0.183	0.201

**Fig. 4.** Configuration of the plane Poiseuille flow.

no-slip boundaries at the top and the bottom. Understandably, the presence of thin solid regions in the former case makes its flow domain slightly narrower than the latter case. But, this reduction in flow area has been accounted here while comparing with the exact analytical solution.

#### 4. Grid independence study

As the resultant discretisation error of any computation is dependent on the mesh used, it becomes mandatory to arrive at an optimum grid for which the error is minimal. However, in the present investigations involving objects of various aspect ratios, arriving at such a single optimum grid is extremely difficult. Even if obtained, it would be associated with the case of largest aspect ratio ( $AR = 5$ ) and may pose computational extravagance for smaller aspect ratio cases. Hence, a different approach has been used in the current work that utilises a non-dimensional value of grid density ( $\zeta = D/\Delta y_{\min}$ ) in the bounding box for each of the aspect ratios. The values of  $C_D$  and  $C_L$  obtained for two aspect ratios ( $AR = 0.5, 1$ ) and different  $\zeta$  ( $= 20, 30$  and  $40$ ) are listed in Table 3. From the table, it is evident that for  $\zeta = 40$ , the variations of  $C_D$ ,  $C_L$  are negligibly small (less than 1%) and hence all simulations in the present work have been carried out using a grid density of  $\zeta = 40$ .

#### 5. Results and discussions

Using the numerical model thus developed, simulations of flow over triangular prisms are now carried out for two different regimes where the characteristics are primarily two-dimensional and laminar. First, the wake-bubble behaviour and its dependence on aspect ratio are analysed in the sub-critical regime of flow (before the onset of vortex shedding). Following this study, a generalised correlation for the variation of dimensionless bubble length ( $L_b$ ) with  $Re$  has been developed for the cases in which the apex of the triangle faces the approaching flow. Subsequently, the critical value of  $Re$  at which the onset of vortex shedding takes place is identified for both the apex- and base-facing configurations. Finally, the

unsteady wake characteristics during vortex shedding have been brought out for various values of  $Re$  within the limit of two dimensionalities. The detailed results related to these regimes are now discussed in the ensuing subsections.

### 5.1. Sub-critical regime

In the sub-critical regime, the flow over any bluff body is characterised by the presence of a steady wake bubble whose length undergoes elongation with the increase in the Reynolds number. In this regard, Zdravkovich (1997) had identified a linear correlation between the bubble length and  $Re$  for flow past circular cylinders. Such a behaviour was also observed for the bluff body with equilateral triangular cross-section by De and Dalal (2006). As can be inferred from these studies, a strong dependence exists between the correlation coefficients and the geometry of the bluff-body. In order to establish such a relationship for the triangular prisms, simulations have been carried out in the present study for seven different aspect ratios ( $AR=0.5, 0.866, 1, 2, 3, 4, 5$ ) at low values of  $Re$  ( $=10, 20, 30, 40$  and  $50$ ). Correspondingly, the computed recirculation length ( $L_r$ ) and its variation with  $Re$  are shown in Fig. 5.

Akin to the case of circular cylinders, Fig. 5 clearly reveals a linear dependence between  $L_r$  and  $Re$  at all the aspect ratios considered. The predictions from the present study are in close agreement with the results of De and Dalal (2006) for  $AR=0.866$  corresponding to the equilateral triangular shape. For a fixed  $Re$ , a monotonic decrease in  $L_r$  is observed here with the increase in aspect ratio. Such an effect can be attributed to the extent of streamline deflection occurring by the virtue of object's shape (illustrated in Fig. 6 for three different aspect ratios and  $Re=40$ ). Evidently, the streamline deflection in each case is approximately equal to the apex half-angle. So, in the case of systems with lower aspect ratio, the deviation in the streamlines path is large since its apex half-angle is large (Fig. 6(a)). This results in a longer re-attachment distance thereby forming a bigger wake bubble. With the increase in aspect ratio (i.e. reduction of apex half-angle), there is a corresponding decrease in  $L_r$  which is evident for the cases of  $AR=3$  and  $AR=5$  in Fig. 6. Additionally as observed in Fig. 5, the rate of reduction in  $L_r$  decreases at higher  $AR$ , as the respective rate of change in the apex half-angle also diminishes. The above manifestation can also be construed as a result of higher shear force encountered by the fluid particles as they glide along the surface of the higher  $AR$  triangle. Resultantly, the associated momentum loss for the particles travelling closer to the surface is severe and so, the strength of the vortex formed behind the object decreases thereby shrinking the size of the vortex bubble.

As already mentioned, the dimensionless wake bubble length ( $L_r$ ) follows a linear relation with  $Re$  of the form  $L_r = k Re$ . The values of the coefficient ' $k$ ' obtained for various aspect ratios considered in the current study are given in Table 4. From the reduction of slope values, it is once again evident that the length of wake monotonically decreases with the aspect ratio

**Table 3**  
Grid independence study for flow over a stationary triangular cylinder at  $Re=200$ .

Grid density (of box enclosure), $\zeta$	$C_D$		$C_{L, rms}$	
	$AR=0.5$	$AR=1.0$	$AR=0.5$	$AR=1.0$
20	2.737	2.023	0.375	0.565
30	2.672	2.052	0.367	0.570
40	2.653	2.077	0.369	0.556

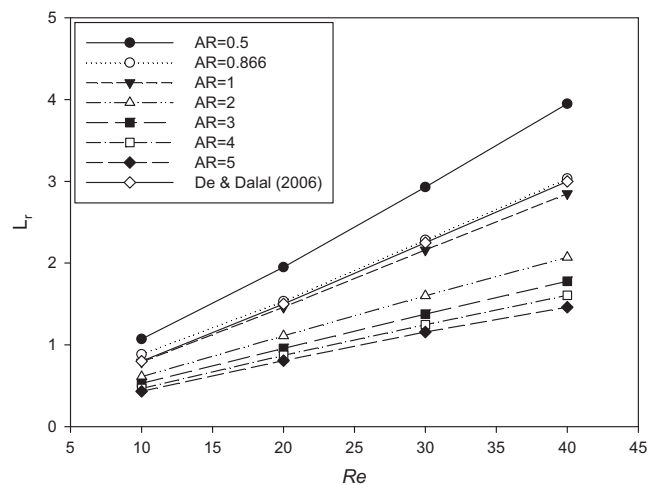


**Fig. 5.** Variation of dimensionless wake bubble length with  $Re$  for various aspect ratios when apex faces the approach flow.



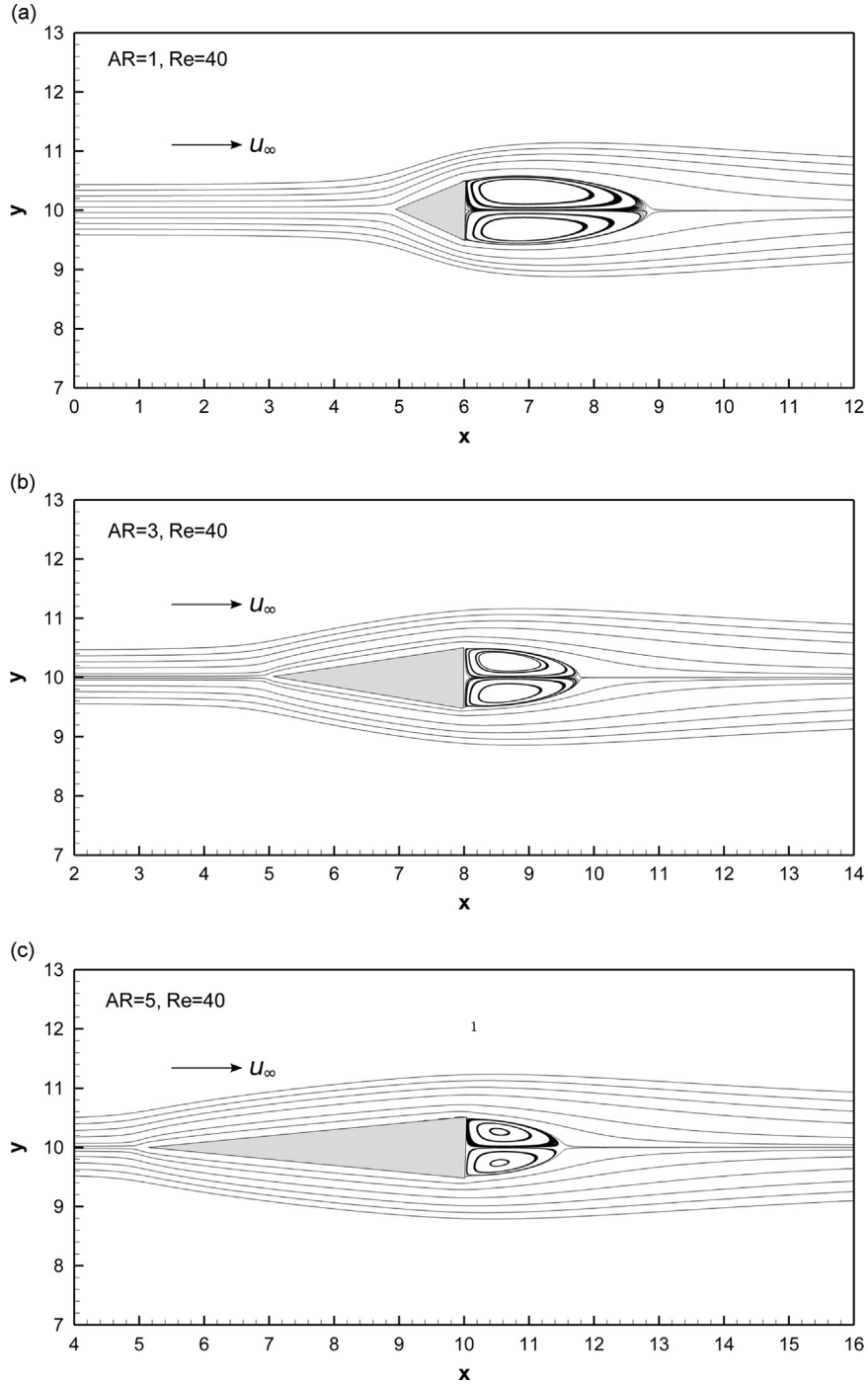


Fig. 6. Streamlines for three different aspect ratios when apex of the triangle faces the flow: (a)  $AR=1$ , (b)  $AR=3$ , and (c)  $AR=5$  at  $Re=40$ .

of the triangle. This dependence of slope values on  $AR$  can be expressed as an exponential function by a least-square fitting process. A suitable form of function for relating the ' $k$ ' and  $AR$  values of Table 4 is given as

$$k = 0.04 + 0.099 \exp(-1.12 AR). \quad (10)$$

The above fit predicts ' $k$ ' values with a deviation of about  $\pm 4\%$  for the range of aspect ratios considered.

Fig. 7(a) and (b) shows the transient evolution of drag coefficient ( $C_D$ ) value on a triangular prism of  $AR=1$  when it is placed in apex- and base-facing configurations respectively. Evidently, for both these configurations, the asymptotic (steady-state)  $C_D$  value decreases when the  $Re$  is increased. This is mainly due to the dominance of skin-friction drag in the sub-

**Table 4**  
Linear fit of  $L_r$  vs Re for different values of AR.

AR	Constant of proportionality, $k$
0.5	0.098
0.866	0.076
1.0	0.071
2.0	0.053
3.0	0.045
4.0	0.041
5.0	0.039

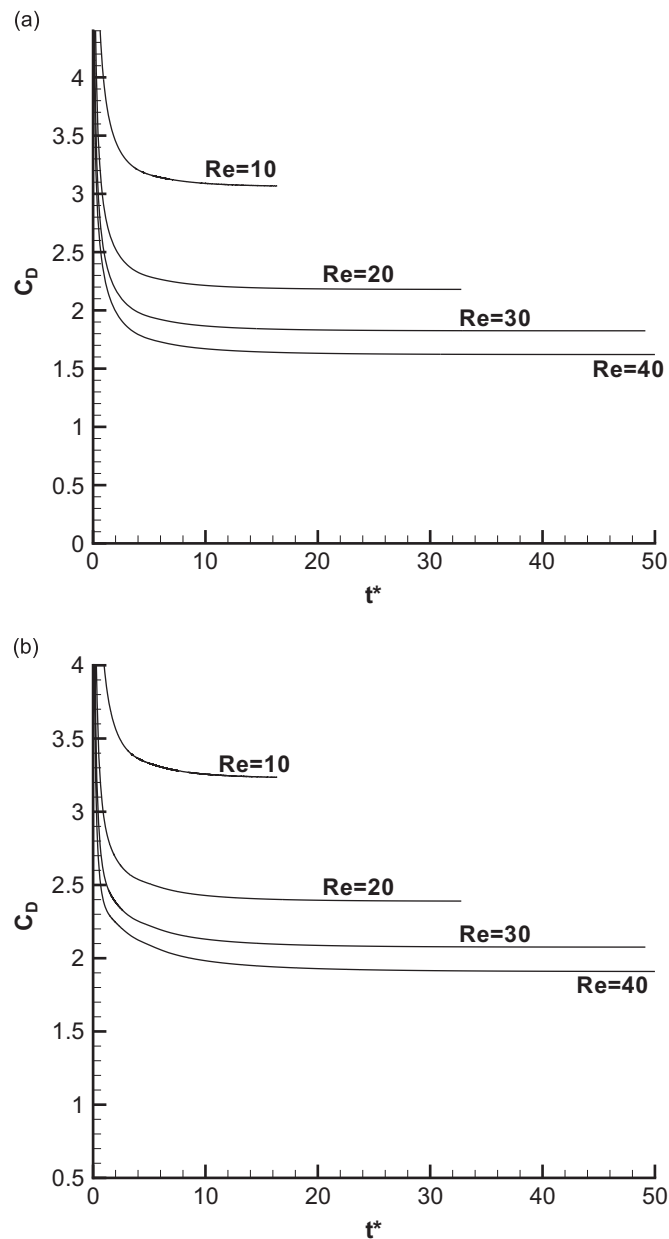


**Fig. 7.** Temporal variation of  $C_D$  at different Re in the sub-critical regime for AR=1: (a) apex facing the flow and (b) base facing the flow.

critical regime, whose relative contribution reduces on the enhancement of inertial forces at higher velocities. In order to understand the AR effects, the asymptotic  $C_D$  values obtained at different AR and Re for the two configurations are now collectively represented in Fig. 8(a) and (b). Interestingly, at all the values of Reynolds numbers, the value of  $C_D$  undergoes an initial decrease followed by a gradual ramp-up with the increase in aspect ratio. The reason for the occurrence of such minima can once again be understood from Fig. 6 where larger wake bubbles are formed at smaller AR. Correspondingly, at the smallest AR, the Reynolds number dependent form-drag component will be significant as compared to the skin friction drag. As the bubble length undergoes reduction with the increase in AR, this form-drag component proportionally reduces while the geometry dependent skin friction drag increases simultaneously. The resultant trade-off between these components leads to a minimum of  $C_D$  whose occurrence shifts to higher AR as the Reynolds number is increased.

## 5.2. Critical regime

Upon increasing the value of Re from the sub-critical regime, the wake bubble attains a state at which it becomes vulnerable to shear-layer instabilities and starts shedding vortices. In order to arrive at the Re value of this transition, the present study uses a technique of extrapolating  $C_{L,max}$  values from a dynamic flow regime that is not far away from the  $Re_{cr}$ . Since such a flow regime is not known a priori, it is found by inspecting flow behaviours at regular intervals of Re starting from the sub-critical regime. Once a narrow regime of transition is identified,  $C_{L,max}$  values are obtained at various Re sub-intervals within this regime. Using the non-trivial values of  $C_{L,max}$  obtained, a linear extrapolation procedure is employed (Zielinska and Wesfreid, 1995) to find out the  $Re_{cr}$  value at which  $C_{L,max}$  is zero. The predicted values of  $Re_{cr}$  for both the apex-facing and base-facing cases are shown in Fig. 9. In the apex-facing scenario, a gradual increase of  $Re_{cr}$  is observed with respect to AR. The reason for such behaviour can be directly deduced from the variation of bubble length with AR (Fig. 5). As the AR value is increased, the growth rate of recirculation length is decreased and so, the Re for the attainment

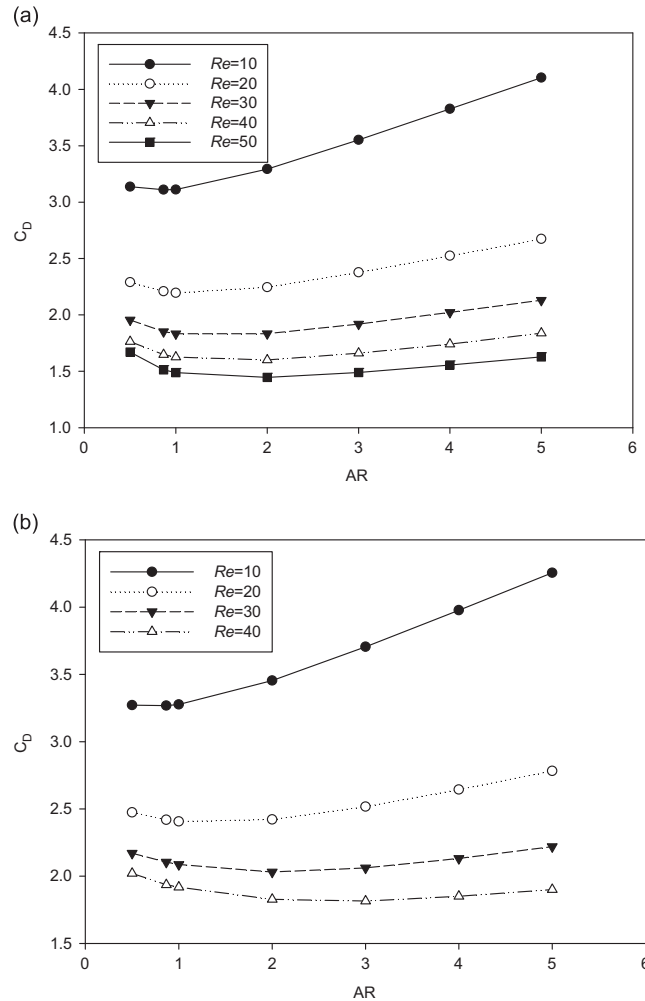
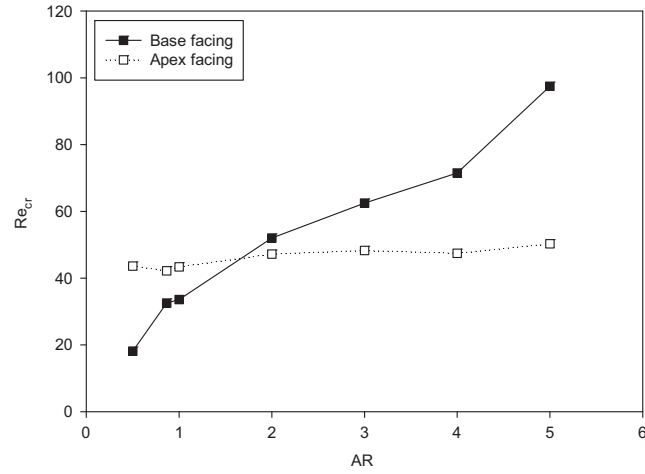
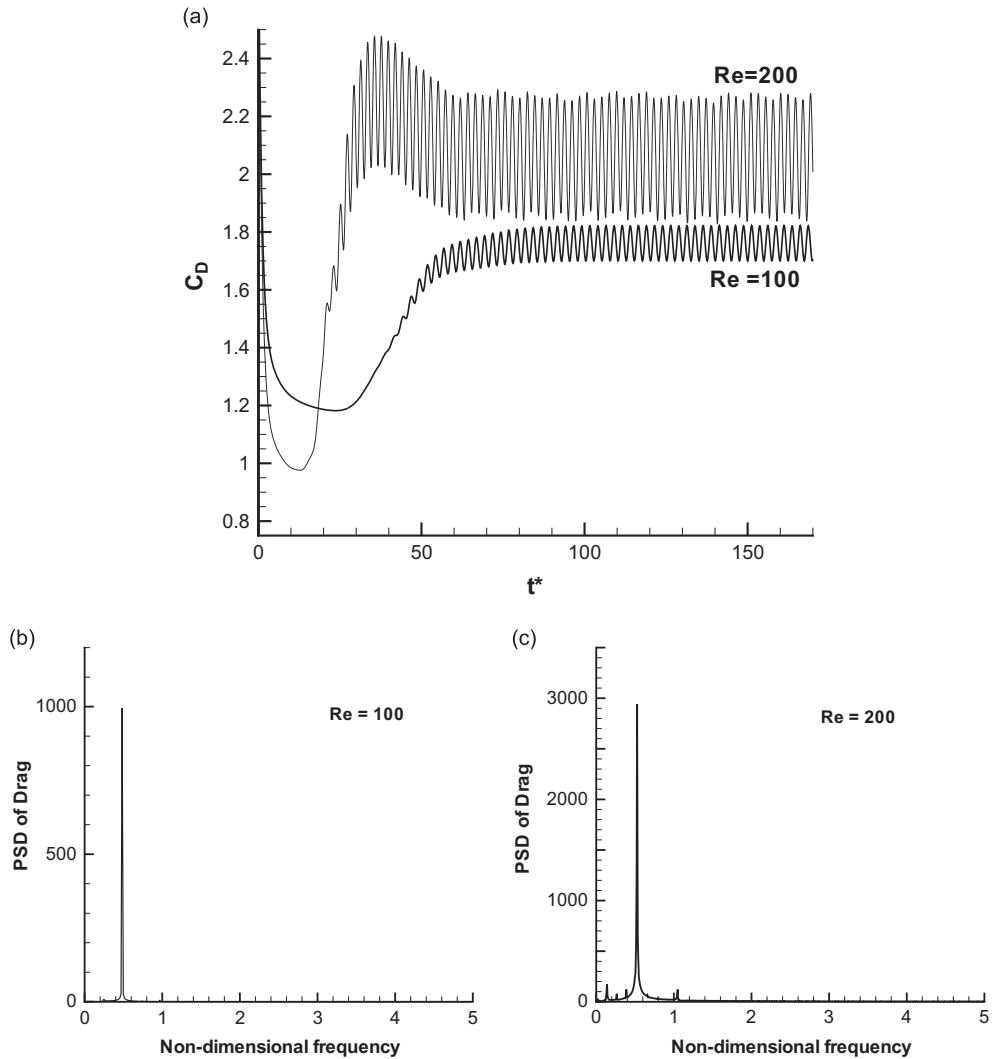


Fig. 8. Variation of  $C_D$  with Re in the sub-critical regime: (a) apex facing the flow and (b) base facing the flow.



**Fig. 9.** Critical Reynolds number computed for different ARs for both apex and base facing the flow.



**Fig. 10.** (a) Temporal variation of  $C_D$  at different  $Re$  in the super-critical regime for  $AR=1$  and apex facing the flow; (b) PSD of  $C_D$  at  $Re=100$  from (a); and (c) PSD of  $C_D$  at  $Re=200$  from (a).

of critical wake length (i.e starting point of shedding) increases. On the other hand, the scenario of base facing the approach flow manifests no steady recirculation and consequently, eddies combine at the tail end of the geometry. In the case of higher AR, the momentum loss induced by the bluff body tail region makes the flow steady. This enhances the stability of flow even at higher velocities, despite the occurrence of flow separation at the corners of the triangle. The plot (Fig. 9) clearly highlights the larger delay in the onset of vortex shedding for the base-facing case.

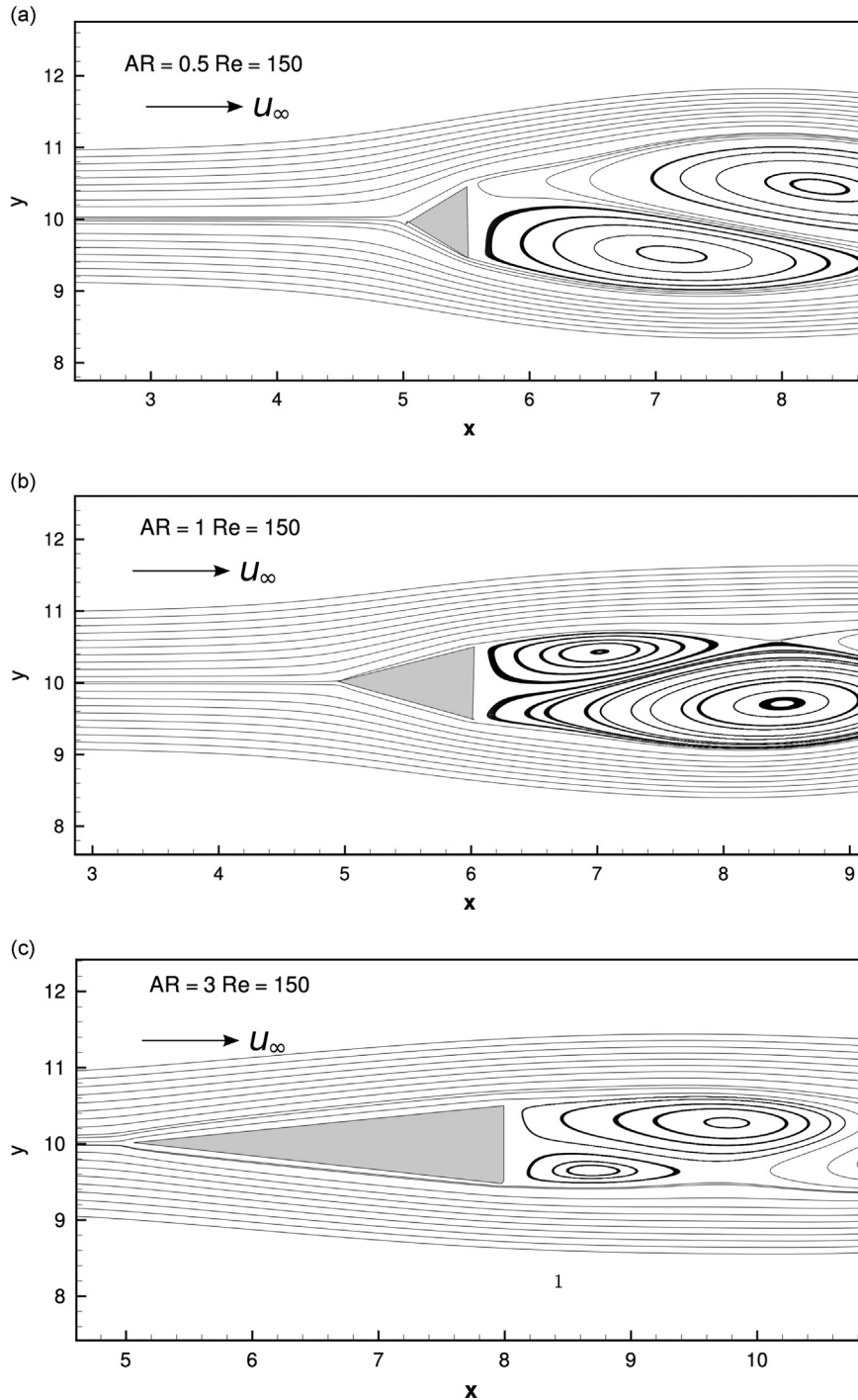


**Fig. 11.** Instantaneous streamlines for three different aspect ratios when apex of the triangle faces the approaching flow at a non-dimensionalised time of 12 500: (a)  $AR=0.5$ , (b)  $AR=1$ , (c)  $AR=3$ , for  $Re=150$ .

### 5.3. Super-critical regime

When the flow velocity exceeds the value corresponding to the critical Reynolds number, the wake flow transits into the super-critical regime where the flow behaviour is dominated by its dynamic nature. Here, the alternate vortex shedding is primarily influenced by the orientation and the geometry (specifically, AR) of the body. In order to understand their characteristics, four values of Reynolds numbers corresponding to the super-critical regime, viz.  $Re = 100, 150, 200, 250$  have been considered in the present analysis. The dynamically varying force coefficients obtained in these cases are additionally utilised to elucidate the aspect ratio effects.

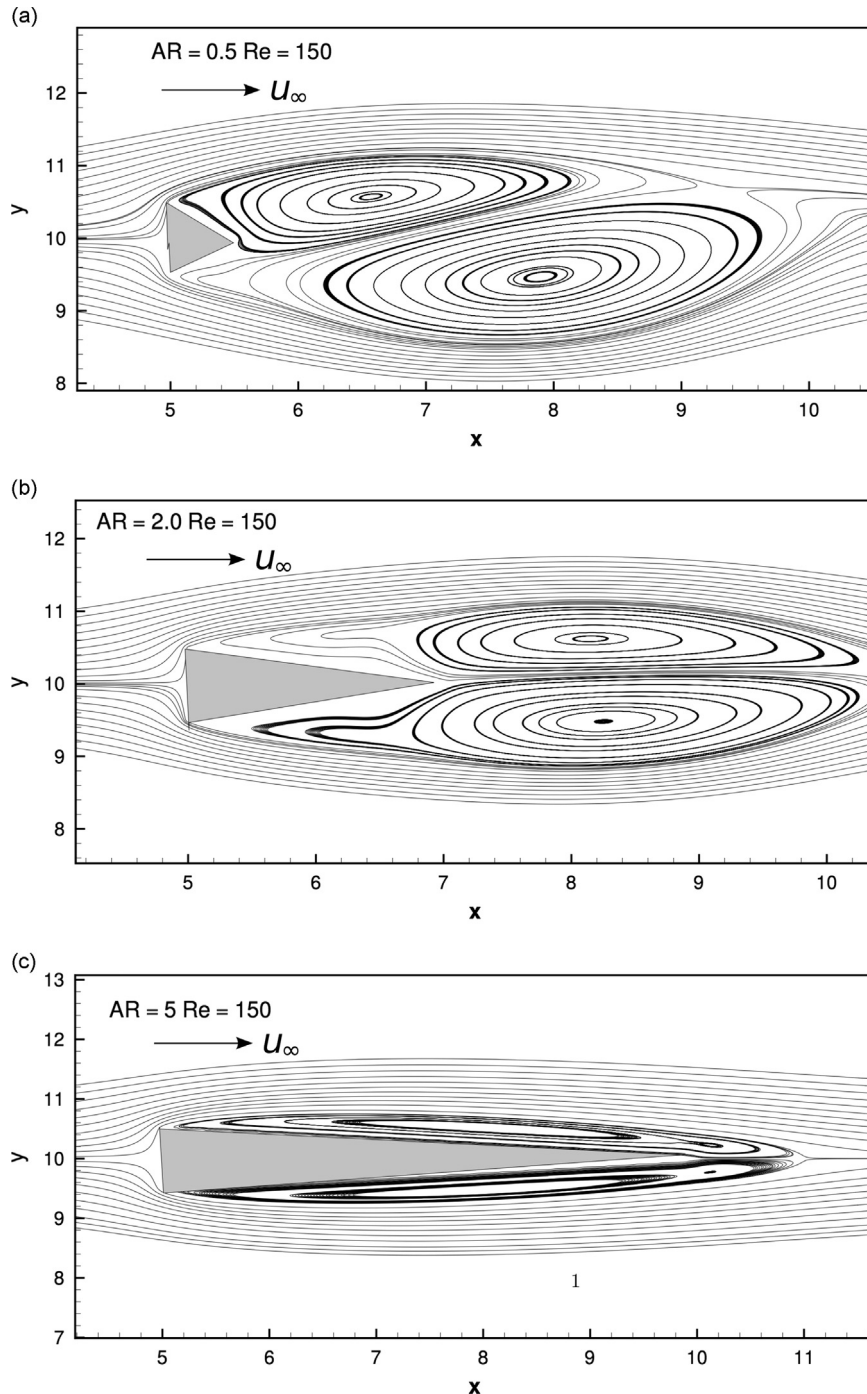


**Fig. 12.** Instantaneous streamlines for three different aspect ratios when base of the triangle faces perpendicular to the flow at a non-dimensionalised time of 12 500: (a)  $AR = 0.5$ , (b)  $AR = 0.866$ , (c)  $AR = 5$ , for  $Re = 150$ .



Fig. 10 shows the temporal fluctuations of  $C_D$  value and its power spectral density (PSD) for super-critical flow over a triangular prism with  $AR=1$  and its apex facing the approaching flow. In contrast to the behaviour in the sub-critical regime, an increase in the mean  $C_D$  value is observed with the increase in  $Re$ . This is primarily due to the dominance of form drag in the super-critical regime which increases in proportion with the  $Re$ . The influence of  $AR$  in this regime can be understood from Figs. 11 and 12, which show the instantaneous streamline patterns observed at various  $AR$  for both the apex-facing and base-facing configurations of the triangular prism. Akin to the effects manifested at lower  $Re$  (Fig. 6), the size of the wake region in all these cases seems to decrease with the increase in  $AR$ . A direct outcome of this behaviour is felt in the drag force, since it is related to the size of momentum deficit zone behind the object. Correspondingly, a reduction in values of  $C_D$  at lower  $AR$  ( $AR < 3$ ) is clearly evident from Fig. 13(a) where the variation of hydrodynamic drag coefficient for the apex-facing scenario is presented. In this case, the drag force behaviour is typically governed by two factors. The first one concerns the gradual decrease of form drag by virtue of reduction in the wake zone as discussed earlier. This is contrasted by the skin-friction drag which increases in proportion with  $AR$ , as the corresponding distance travelled by the fluid particles along the walls increases. As a trade-off between these two factors, a local minimum is observed for  $C_D$  at a unique value of  $AR$  for a given  $Re$ . With the increase in  $Re$ , the form drag component is increased and hence, the point of local minimum is shifted to a higher value of  $AR$ .

A similar behaviour is also observed in Fig. 13(b) which shows the characteristic decrease in the  $C_D$  values with the increase in  $AR$  for the base-facing case. Interestingly, for the values of  $AR$  considered in the current case, only a monotonic decrease in the  $C_D$  values is observed. This is mainly due to the separation of approach-flow from the rear walls by the presence of wake zones. With the increase in  $AR$ , the separated flow zone begins to shrink and hence, there is a corresponding decrease in the drag coefficient. At a value of  $AR$  beyond those considered in the current work, the size of wake zones would be small enough to allow re-attachment of approach flow streamlines to the walls. From this point, the  $C_D$  values are expected to increase by virtue of higher skin-friction drag. Thus, it would be reasonable to anticipate a local minimum for  $C_D$  at a larger  $AR$ , resembling the flow behaviour for apex-facing cases.

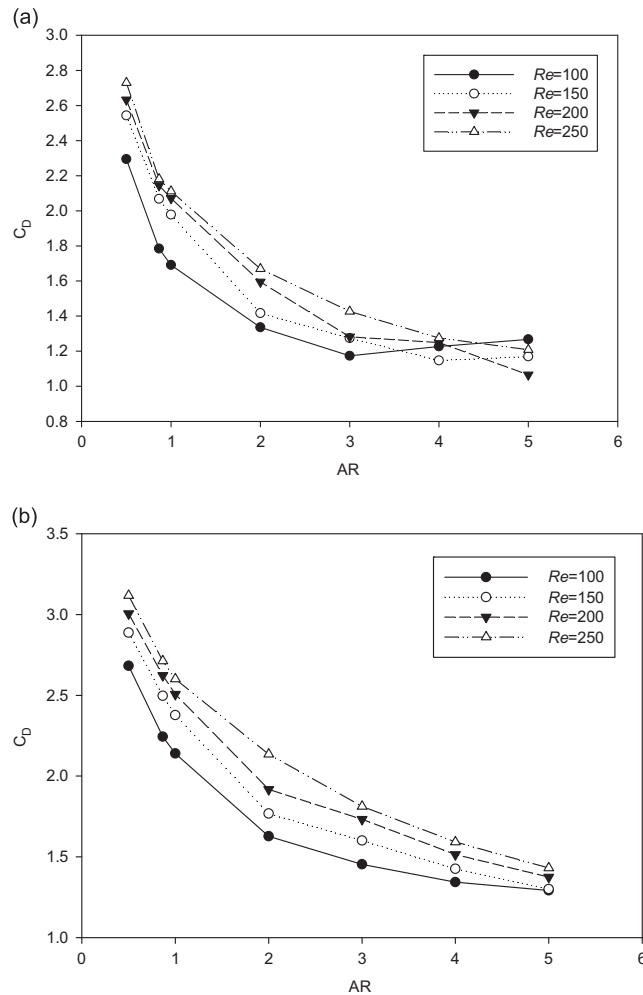


Fig. 13. Variation of time averaged  $C_D$  with  $Re$  in the super-critical regime: (a) apex facing the flow and (b) base facing the flow.

The temporal variations of  $C_L$  values corresponding to the exact parameters of Fig. 10 are shown in Fig. 14. Predictably, the phenomena of alternate vortex shedding make the peak in PSD of  $C_L$  to occur at half the frequency corresponding to the peak in  $C_D$  value.

The influences of prism aspect ratio on the lift coefficient ( $C_{L,rms}$ ) for both the apex-facing and base-facing cases are shown in Fig. 15. Despite a few oddities at certain AR and Re combinations, the overall behaviour of these curves fits onto a general trend of gradual increase which is followed by an asymptotic decrease. The initial increase in the  $C_{L,rms}$  value is a direct consequence of the increase in projected area of the prism in the lateral  $y$ -direction (proportional to the prism height  $h$ ). In the regime of smaller AR ( $AR < 3$ ), the effect due to larger projected area is dominant over the reduction in wake size; however, around the value of  $AR=3$ , the influence of reduction in wake size begins to overwhelm the increase in projected area which results in an asymptotic decrease in the  $C_{L,rms}$  value. It is important to note here that the lift coefficients for the base-facing case (Fig. 15(b)) are much higher as compared to those of the apex-facing case (Fig. 15(a)). This is mainly due to the direct impact of eddies on the surfaces of the base-facing prism.

## 6. Conclusion

The present study investigates the wake features of laminar flow over a triangular prism in different flow regimes. Both apex and base facing configurations of the prism have been considered for various aspect ratios. A fixed grid formulation has been employed with a Carman–Koseny type source term in the momentum equation to emulate the presence of solid

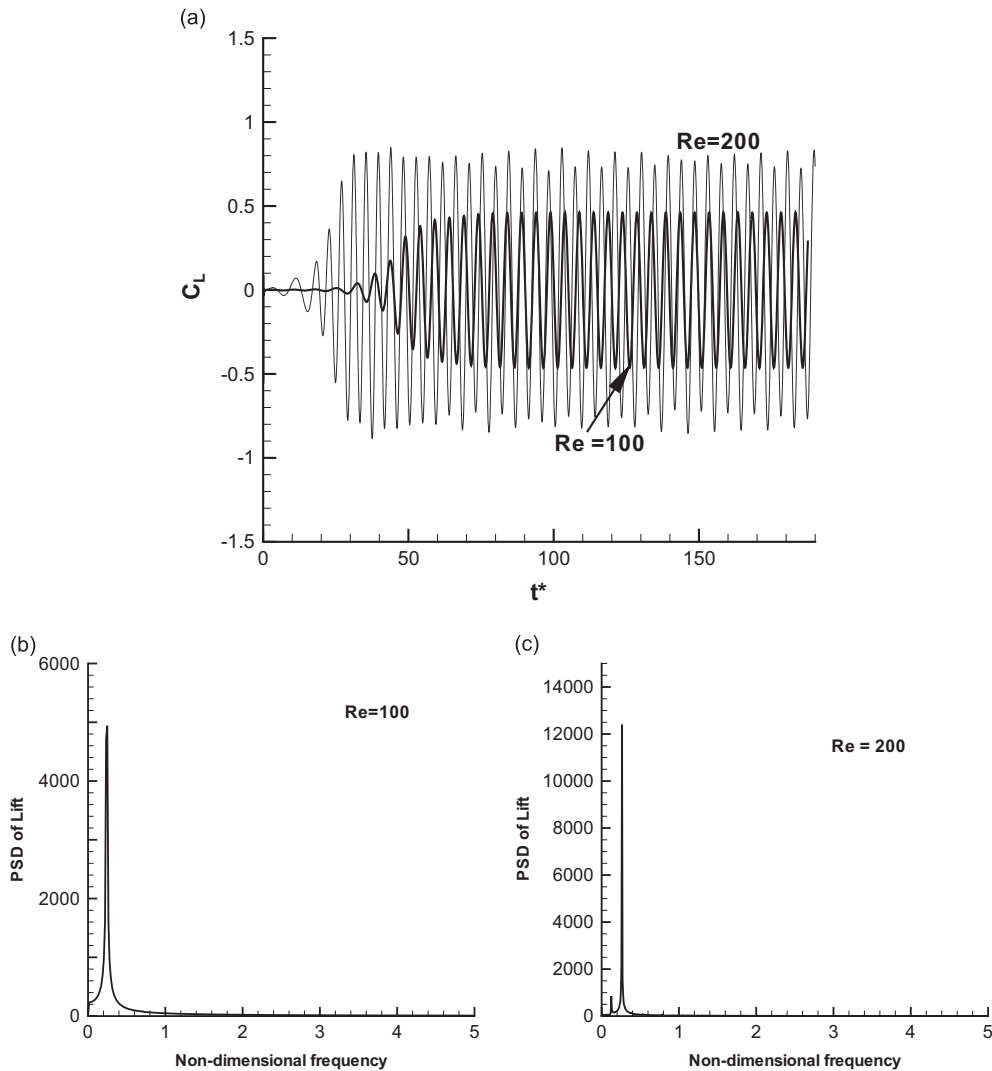


**Fig. 14.** (a) Temporal variation of  $C_L$  at different Re in the super-critical regime for AR=1 and apex facing the flow; (b) PSD of  $C_L$  at Re=100 from (a); and (c) PSD of  $C_L$  at Re=200 from (a).

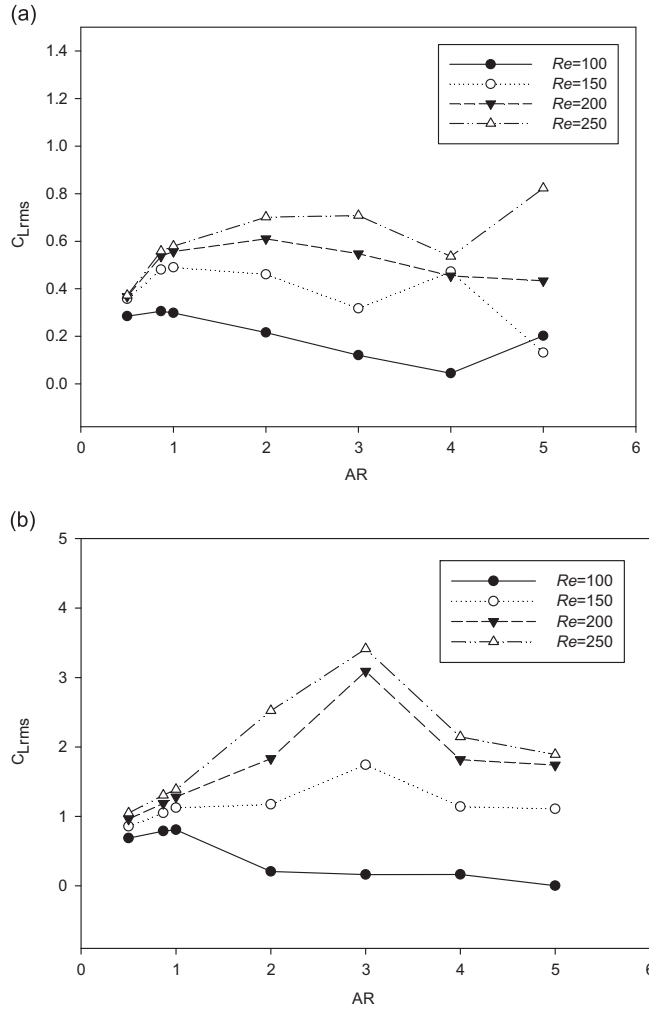


Fig. 15. Variation of  $C_{L,rms}$  with  $Re$  in the super-critical regime: (a) apex facing the flow and (b) base facing the flow.

obstruction. By means of this volumetric forcing, the behaviour of flow over triangular prisms has been obtained here without any spurious flow fields. In addition, the need for explicit specification of conditions at the solid surface is eliminated in the current approach. Owing to the simple nature of the source term, the current method has all the feasibility for extension to three dimensions and is also capable of predicting turbulent flows after suitable mesh refinement in the interfacial region.

With regard to the physics of flow over triangular prisms, linear dependence of vortex bubble length on Reynolds number has been observed in the sub-critical regime, when the apex of the prism faces the approaching flow. This is quite similar to the behaviour observed for circular cylinders. However, an exponentially decaying behaviour is observed when the aspect ratio of the prism is gradually increased. This decaying nature has been attributed to the strength of the vortex formed behind the prism which in turn is affected by the deceleration of fluid particles as they glide through longer distance in higher AR cases. Subsequently, the effect of aspect ratio on the critical Reynolds number has been obtained for both the configurations. In general, a delay in the onset of vortex shedding is observed upon increasing the prism aspect ratio; however, its influence is more prominent for the base facing configuration. This was due to the momentum loss created by the bluff body's tail that made the flow steady. Resultantly, the base-facing prism systems have larger  $Re_{cr}$  than apex-facing cases at scenarios beyond  $AR=2$ . Hence for all practical purposes, it may be necessary to choose the right configuration (either apex-facing or base-facing) of the prism based on the requirements of criticality in the system. In other words, for applications requiring delayed onset of criticality, a choice of apex-facing configuration may be favourable when the AR of the prism is  $> 2$ . For cases with  $AR > 2$ , utilisation of the base-facing case is advisable. In the super-critical regime, the trade-off between the form drag and the skin friction drag was found to result in minima of  $C_D$  value with respect to the AR. Incidentally, this point of minimum  $C_D$  was found to move to a higher AR as the Reynolds number of the flow was increased. Hence, it is not possible to find a unique value of AR for which  $C_D$  is minimum for all the  $Re$  values considered. On the other

hand, the RMS lift has a notable point of maxima with respect to AR (around  $AR=3$ ). The trade-off in this case was found to arise from the increase in projected area of the object and the reduction in wake size as the aspect ratio of the prism is increased.

## References

- Abbassi, H., Turki, S., Ben Nasrallah, S., 2001. Numerical investigation of forced convection in a plane channel with a built-in triangular prism. *International Journal of Thermal Sciences* 40 (7), 649–658.
- Angot, P., Bruneau, C., Fabrie, P., 1999. A penalization method to take into account obstacles in incompressible viscous flows. *Numerische Mathematik* 81 (4), 497–520.
- Bao, Y., Zhou, D., Zhao, Y.J., 2010. A two-step Taylor-characteristic-based Galerkin method for incompressible flows and its application to flow over triangular cylinder with different incidence angles. *International Journal for Numerical Methods in Fluids* 62, 1181–1208.
- Braza, M., Chassaing, P., Minh, H., 1986. Numerical study and physical analysis of the pressure and velocity fields in the near wake of a circular cylinder. *Journal of Fluid Mechanics* 165, 79–130.
- Brinkman, H., 1949. A calculation of the viscous force exerted by a flowing fluid on a dense swarm of particles. *Applied Scientific Research* 1 (1), 27–34.
- Calhoun, D., 2002. A Cartesian grid method for solving the two-dimensional streamfunction-vorticity equations in irregular regions. *Journal of Computational Physics* 176, 231–275.
- Carman, P., 1937. Fluid flow through granular beds. *Transactions—Institution of Chemical Engineers* 15, 150–166.
- Davis, R., Moore, E., 1982. A numerical study of vortex shedding from rectangles. *Journal of Fluid Mechanics* 116, 475–506.
- De, A.K., Dalal, A., 2006. Numerical simulation of unconfined flow past a triangular cylinder. *International Journal of Numerical Methods in Fluids* 52, 801–821.
- De, A.K., Dalal, A., 2007. Numerical study of laminar forced convection fluid flow and heat transfer from a triangular cylinder placed in a channel. *Journal of Heat Transfer* 129, 646–656.
- Fey, U., König, M., Eckelmann, H., 1998. A new Strouhal–Reynolds-number relationship for the circular cylinder in the range  $47 < Re < 2 \times 10^5$ . *Physics of Fluids* 10, 1547.
- Goldstein, D., Handler, R., Sirovich, L., 1993. Modeling a no-slip flow boundary with an external force field. *Journal of Computational Physics* 105 (2), 354–366.
- Iungo, G., Buresti, G., 2009. Experimental investigation on the aerodynamic loads and wake flow features of low aspect-ratio triangular prisms at different wind directions. *Journal of Fluids and Structures* 25 (7), 1119–1135.
- Kelkar, K., Patankar, S., 1992. Numerical prediction of vortex shedding behind square cylinders. *International Journal of Numerical Methods in Fluids* 14, 327–341.
- Khadra, K., Angot, P., Parneix, S., Caltagirone, J., 2000. Fictitious domain approach for numerical modelling of Navier–Stokes equations. *International Journal of Numerical Methods in Fluids* 34 (8), 651–684.
- Lai, M., Peskin, C., 2000. An immersed boundary method with formal second-order accuracy and reduced numerical viscosity. *Journal of Computational Physics* 160 (2), 705–719.
- Le, D., Khoo, B., Lim, K., 2008. An implicit-forcing immersed boundary method for simulating viscous flows in irregular domains. *Computational Methods in Applied Mechanical Engineering* 197, 2119–2130.
- Leonard, B., 1979. A stable and accurate convective modelling procedure based on quadratic upstream interpolation. *Computer Methods in Applied Mechanics and Engineering* 19 (1), 59–98.
- Peskin, C., 1972. Flow patterns around heart valves: a numerical method. *Journal of Computational Physics* 10 (2), 252–271.
- Roshko, A., 1954. On the development of turbulent wakes from vortex streets. *National Advisory Committee for Aeronautics Report* 19, 59–98.
- Shanks, S., Thompson, J., 1977. Coupling genetic algorithms and gradient based optimization techniques. In: *Proceedings of the Second International Conference on Numerical Ship Hydrodynamics*, Berkeley, pp. 202–220.
- Shyamprasad, N.R., Diwakar, S.V., Tiwari, S., Sundararajan, T., 2011. Numerical simulation of external flows around oscillating rigid bodies using a novel fixed Cartesian grid methodology. In: *Proceedings of the International Union of Theoretical Applied Mechanics Symposium on Bluff Body Flows*, pp. 163–166.
- Silva, L., Silveira-Neto, A., Damasceno, J., 2003. Numerical simulation of two-dimensional flows over a circular cylinder using the immersed boundary method. *Journal of Computational Physics* 189 (2), 351–370.
- Sinha, S., Sundararajan, T., Garg, V., 1992. A variable property analysis of alloy solidification using the anisotropic porous medium approach. *International Journal of Heat and Mass Transfer* 35 (11), 2865–2877.
- Sriragom, S., Koh, A., 2008. Flow field of self-excited rotationally oscillating equilateral triangular cylinder. *Journal of Fluids and Structures* 24 (5), 750–755.
- Srikanth, S., Dhiman, A., Bijjam, S., 2010. Confined flow and heat transfer across a triangular cylinder in a channel. *International Journal of Thermal Sciences* 49 (11), 2191–2200.
- Su, S., Lai, M., Lin, C., 2007. An immersed boundary technique for simulating complex flows with rigid boundary. *Computers and Fluids* 36 (2), 313–324.
- Sumner, D., 2010. Two circular cylinders in cross-flow: a review. *Journal of Fluids and Structures* 26 (6), 849–899.
- Thompson, M., Lewke, T., Williamson, C., 2001. The physical mechanism of transition in bluff body wakes. *Journal of Fluids and Structures* 15 (3–4), 607–616.
- Van der Vorst, H., 1992. Bi-CGSTAB: a fast and smoothly converging variant of Bi-CG for the solution of nonsymmetric linear systems. *SIAM Journal on Scientific and Statistical Computing* 13, 631.
- Voller, V., Prakash, C., 1987. A fixed grid numerical modelling methodology for convection-diffusion mushy region phase-change problems. *International Journal of Heat and Mass Transfer* 30 (8), 1709–1719.
- Williamson, C., 1989. Oblique and parallel modes of vortex shedding in the wake of a circular cylinder at low Reynolds numbers. *Journal of Fluid Mechanics* 206, 579–627.
- Williamson, C., 1996. Vortex dynamics in the cylinder wake. *Annual Reviews of Fluid Mechanics* 28, 477–539.
- Xu, S., Wang, J., 2006. An immersed interface method for simulating the interaction of a fluid with moving boundaries. *Journal of Computational Physics* 216, 454–493.
- Zdravkovich, M., 1990. Conceptual overview of laminar and turbulent flows past smooth and rough circular cylinders. *Journal of Wind Engineering and Industrial Aerodynamics* 33, 53–62.
- Zdravkovich, M., 1997. *Flow Around Circular Cylinders*. Oxford University Press, New York.
- Zeitoun, O., Ali, M., Nuhait, A., 2011. Convective heat transfer around a triangular cylinder in an air cross flow. *International Journal of Thermal Sciences* 50 (9), 1685–1697.
- Zielinska, B.J.A., Wesfreid, J.E., 1995. On the spatial structure of global modes in wake flow. *Physics of Fluids* 7 (6), 1418–1424.